LIQUID CRYSTALS, 2003, VOL. 30, NO. 3, 367–375

Taylor & Francis
Taylor & Francis Group

Optical wave propagation in a cholesteric liquid crystal using the finite element method

QI HONG, THOMAS X. WU
School of Electrical Engineering and Computer Science,
University of Central Florida, Orlando, FL 32816, USA

and SHIN-TSON WU*
School of Optics/CREOL, University of Central Florida, Orlando, FL 32816, USA

(*Received 30 September 2002; accepted 1 November 2002*)

Bragg reflections of cholesteric liquid crystals at normal and oblique incidences were investigated using the finite element method (FEM). Detailed FEM derivations together with the consideration of boundary conditions are given. Two methods for achieving broadband Bragg reflection are analysed: one is to use high birefringence liquid crystal in the uniform pitch structure, the other is to use the gradient pitch structure. In each case, the number of cholesteric pitches required for establishing the Bragg reflection was simulated.

1. Introduction

A broadband cholesteric liquid crystal (Ch-LC) has important applications for reflective displays and diffusive reflectors and reflective polarizers [1–3]. The Ch-LC cell is typically prepared by doping some chiral agents into a nematic LC mixture. Such cholesteric structure is periodic around a preferred axis and the spatial period is equal to half of the pitch length P_0. The Bragg reflection of the incident light occurs around the central wavelength $\lambda_0 = nP_0$. Only the incident light with the same circular polarization as the cholesteric helix is strongly reflected, and the opposite circular polarization is transmitted without any significant reflection. This scattering depends on the birefringence and the chiral arrangement of the rod-shape molecules [1–9].

To analyse the light propagation in the cholesteric medium, the 4×4 matrix method has been developed [10]. The 4×4 matrix method is fast, however it is difficult to be used to solve two-dimensional and three-dimensional problems, especially when the geometry is complex. In this paper, we investigate the Bragg reflection properties of cholesteric LCs using the finite element method (FEM). FEM is a well recognized numerical method since a general purpose computer program can be easily developed to analyse rigorously the problems where analytical solutions are difficult to obtain, e.g. the three-dimensional modelling of liquid crystal devices. Moreover, FEM has the advantages of easy convergence in the space domain, and unconditional convergence and high order error in the time domain, as compared with the finite difference time domain (FDTD) method [11–14], which is another well recognized numerical method in optical simulations. Moreover, the parameter matrices of the differential equation are sparse in the finite element method. If we take the advantage of sparse matrix, the calculation time can be reduced significantly.

To broaden the reflection bandwidth, the high birefringence and gradient pitch methods are commonly used. We apply our finite element method to analyse the reflection bandwidths of these two modes at normal and oblique incidences.

*Author for correspondence; e-mail: swu@mail.ucf.edu

2. Numerical modelling

2.1. *Finite element formulations*

For the cholesteric LC, there is a spiral structure of the liquid crystal directors as shown in figure 1. This chiral structure has a periodicity P_0, which is known as the pitch length. In this case, the dielectric tensor is only a function of the z-coordinate as given by [1]:

$$\varepsilon(z) = \begin{bmatrix} \varepsilon_{11}(z) & \varepsilon_{12}(z) & \varepsilon_{13}(z) \\ \varepsilon_{21}(z) & \varepsilon_{22}(z) & \varepsilon_{23}(z) \\ \varepsilon_{31}(z) & \varepsilon_{32}(z) & \varepsilon_{33}(z) \end{bmatrix} \quad (1)$$

Liquid Crystals ISSN 0267-8292 print/ISSN 1366-5855 online © 2003 Taylor & Francis Ltd
http://www.tandf.co.uk/journals
DOI: 10.1080/0267829031000083777

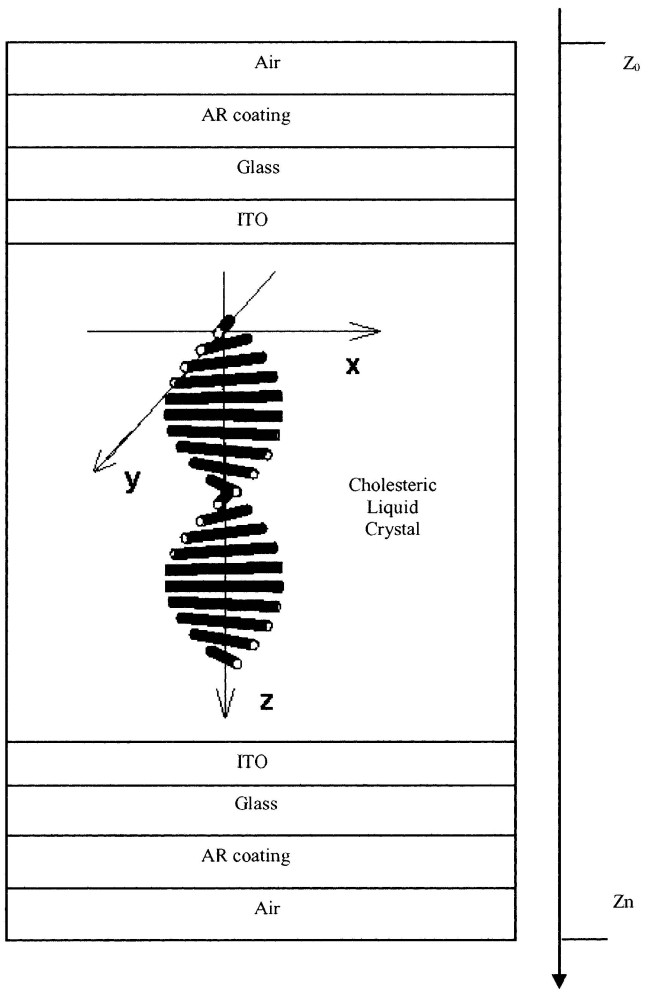

Figure 1. The cholesteric structure used for simulations.

where

$$\varepsilon_{11}(z) = \frac{1}{2}(\varepsilon_{\parallel} + \varepsilon_{\perp}) + \frac{1}{2}(\varepsilon_{\parallel} - \varepsilon_{\perp}) \cos\left(\frac{4\pi}{P_0} z\right)$$

$$\varepsilon_{22}(z) = \frac{1}{2}(\varepsilon_{\parallel} + \varepsilon_{\perp}) - \frac{1}{2}(\varepsilon_{\parallel} - \varepsilon_{\perp}) \cos\left(\frac{4\pi}{P_0} z\right)$$

$$\varepsilon_{12}(z) = \frac{1}{2}(\varepsilon_{\parallel} - \varepsilon_{\perp}) \sin\left(\frac{4\pi}{P_0} z\right)$$

$$\varepsilon_{21}(z) = \varepsilon_{12}(z)$$

$$\varepsilon_{33}(z) = \varepsilon_{\perp}.$$

Here P_0, $\varepsilon_{\parallel}$ and $\varepsilon_{\perp}$ are the cholesteric pitch length, and the dielectric constants perpendicular and parallel to the liquid crystal director, respectively.

In a special case when ε_{13}, ε_{23}, ε_{31} and ε_{32} are equal to zero, the following equations can be derived from Maxwell's equations [1]:

$$\frac{\partial}{\partial z}\begin{bmatrix} E_x \\ E_y \\ H_x \\ H_y \end{bmatrix} = \mathrm{j}k_0 \begin{bmatrix} 0 & 0 & 0 & \eta_0\left(\dfrac{k_x^2}{k_0^2}\dfrac{1}{\varepsilon_{33}} - 1\right) \\ 0 & 0 & \eta_0 & 0 \\ \dfrac{\varepsilon_{21}}{\eta_0} & \dfrac{1}{\eta_0}\left(\varepsilon_{22} - \dfrac{k_x^2}{k_0^2}\right) & 0 & 0 \\ -\dfrac{\varepsilon_{11}}{\eta_0} & -\dfrac{\varepsilon_{12}}{\eta_0} & 0 & 0 \end{bmatrix} \times \begin{bmatrix} E_x \\ E_y \\ H_x \\ H_y \end{bmatrix} = \mathrm{j}k_0 \begin{bmatrix} 0 & \eta_0 \underline{\underline{Q}}_H \\ \dfrac{1}{\eta_0}\underline{\underline{Q}}_E & 0 \end{bmatrix} \cdot \begin{bmatrix} E_x \\ E_y \\ H_x \\ H_y \end{bmatrix} \tag{2}$$

where

$$k_x = k_0 \sin\theta \quad \text{and} \quad \eta_0 = \sqrt{\mu_0/\varepsilon_0}$$

$$\underline{\underline{Q}}_E = \begin{bmatrix} \varepsilon_{21} & \left(\varepsilon_{22} - \dfrac{k_x^2}{k_0^2}\right) \\ -\varepsilon_{11} & -\varepsilon_{12} \end{bmatrix}$$

$$\underline{\underline{Q}}_H = \begin{bmatrix} 0 & \left(\dfrac{k_x^2}{k_0^2}\dfrac{1}{\varepsilon_{33}} - 1\right) \\ 1 & 0 \end{bmatrix}.$$

From equation (2), we can derive the following one-dimensional wave equations for E_x and E_y as

$$\frac{\mathrm{d}}{\mathrm{d}z}\left(\frac{1}{k_0}\underline{\underline{Q}}_H^{-1}\frac{\mathrm{d}}{\mathrm{d}z}\begin{bmatrix} E_x \\ E_y \end{bmatrix}\right) + k_0 \underline{\underline{Q}}_E \begin{bmatrix} E_x \\ E_y \end{bmatrix} = 0. \tag{3}$$

Using the Galerkin method [12] to solve the wave equations, equation (3) is expressed in the weak form as:

$$\int_{z_0^e}^{z_n^e} \left[\left(-\frac{1}{k_0}\underline{\underline{Q}}_H^{-1}\right)\frac{\mathrm{d}W_n}{\mathrm{d}z} \cdot \frac{\mathrm{d}}{\mathrm{d}z}\begin{bmatrix} E_x \\ E_y \end{bmatrix} + k_0 \underline{\underline{Q}}_E W_n \begin{bmatrix} E_x \\ E_y \end{bmatrix}\right] \mathrm{d}z + \frac{1}{k_0}\underline{\underline{Q}}_H^{-1} W_n \frac{\mathrm{d}}{\mathrm{d}z}\begin{bmatrix} E_x \\ E_y \end{bmatrix}\Bigg|_{z=z_0}^{z=z_n} = 0 \tag{4}$$

where W_n is the weighting function.

Applying the finite element method, in the z-direction, the liquid crystal region is discretized by a second order uniform mesh as shown in figure 2. The electric field

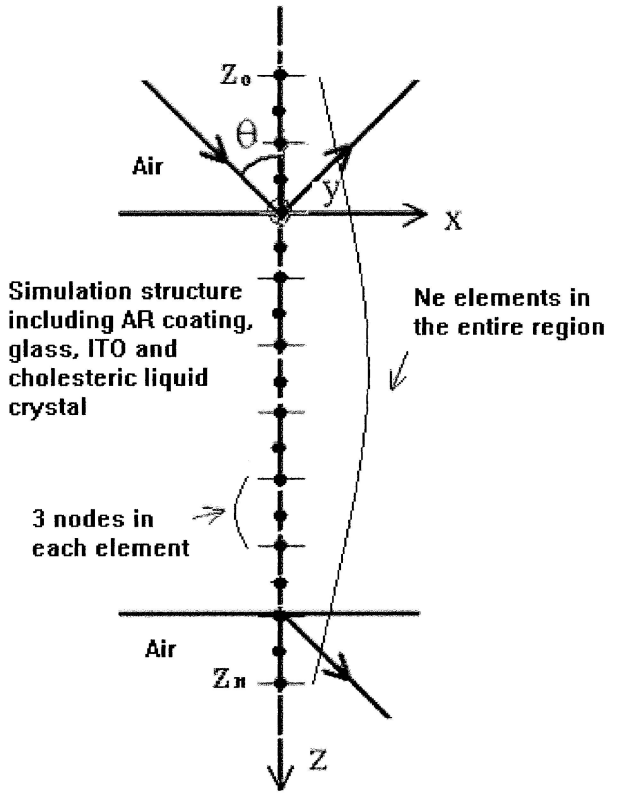

Figure 2. Discretization of the problem region.

intensity is represented in a set of linear equations:

$$\begin{bmatrix} E_x \\ E_y \end{bmatrix} = \sum_{e=1}^{N_e} \sum_{i=1}^{3} \begin{bmatrix} E_x \\ E_y \end{bmatrix}_i^e N_i^e(z) \tag{5}$$

where $[E_x/E_y]_i^e$ are the unknown electric field intensities at the node i of element e that needs to be solved, N_e is the total number of elements and $N_i^e(z)$ are the shape functions defined as:

$$N_1^e(z) = \begin{cases} \dfrac{(z-z_2^e)(z-z_3^e)}{(z_1^e-z_2^e)(z_1^e-z_3^e)}, & z_1^e < z < z_3^e \\ 0 & \text{otherwise} \end{cases}$$

$$N_2^e(z) = \begin{cases} \dfrac{(z-z_1^e)(z-z_3^e)}{(z_2^e-z_1^e)(z_2^e-z_3^e)}, & \\ 0 & \text{otherwise} \end{cases}$$

$$N_3^e(z) = \begin{cases} \dfrac{(z-z_1^e)(z-z_2^e)}{(z_3^e-z_1^e)(z_3^e-z_2^e)}, & z_1^e < z < z_3^e. \\ 0 & \end{cases} \tag{6}$$

In our analysis, we can define the weighting function in equation (4) as $W_n(z) = N_i^e(z)$.

Equation (4) is then repeatedly applied through the whole region for each element as follows:

$$\sum_{e=1}^{N_e} \left\{ \sum_{i=1}^{3} \int_{z_1^e}^{z_3^e} \left[\left(-\frac{1}{k_0} \underline{\underline{Q}}_H^{-1} \right) \frac{\mathrm{d}W_n}{\mathrm{d}z} \cdot \frac{\mathrm{d}}{\mathrm{d}z} \begin{bmatrix} E_x \\ E_y \end{bmatrix} + k_0 \underline{\underline{Q}}_E W_n \begin{bmatrix} E_x \\ E_y \end{bmatrix} \right] \mathrm{d}z \right\} + \frac{1}{k_0} \underline{\underline{Q}}_H^{-1} W_n \frac{\mathrm{d}}{\mathrm{d}z} \begin{bmatrix} E_x \\ E_y \end{bmatrix} \Bigg]_{z=z_0}^{z=z_n} = 0. \tag{7}$$

Applying the weighting function and the shape functions to equation (7) gives

$$\sum_{e=1}^{N_e} \left\{ \sum_{i,j=1}^{3} \begin{bmatrix} E_x \\ E_y \end{bmatrix} \int_{z_1^e}^{z_3^e} \left[\left(-\frac{1}{k_0} \underline{\underline{Q}}_H^{-1} \right) \frac{\mathrm{d}N_i^e(z)}{\mathrm{d}z} \cdot \frac{\mathrm{d}N_j^e(z)}{\mathrm{d}z} + k_0 \underline{\underline{Q}}_E N_i^e(z) N_j^e(z) \right] \mathrm{d}z \right\} + \left[\frac{1}{k_0} \underline{\underline{Q}}_H^{-1}(z) \frac{\mathrm{d}}{\mathrm{d}z} \begin{bmatrix} E_x \\ E_y \end{bmatrix} \Bigg|_{z=z_0} - \frac{1}{k_0} \underline{\underline{Q}}_H^{-1} W_n \frac{\mathrm{d}}{\mathrm{d}z} \begin{bmatrix} E_x \\ E_y \end{bmatrix} \Bigg|_{z=z_n} \right] = 0. \tag{8}$$

The terms outside the summation give us the boundary conditions, by which the incident wave can be applied [12].

Rewriting equation (8) in matrix form gives

$$[A] \cdot [E] = [b] \tag{9}$$

where $[A]$ is a tridiagonal matrix taking the generic spares form. The diagonal entry and its adjacent elements are the only non-zero entries. Equation (9) can be written as:

$$\begin{bmatrix} A_{11}^1 & A_{12}^1 & A_{13}^1 & & & & & & & & \\ A_{21}^1 & A_{21}^1 & A_{23}^1 & \cdots & & 0 & & \cdots & & 0 & \\ A_{31}^1 & A_{32}^1 & A_{33}^1 + A_{11}^2 & & & & & & & & \\ \vdots & & & \ddots & & \vdots & & & & \vdots & \\ & & & & A_{33}^{e-1} + A_{11}^e & A_{12}^e & A_{13}^e & & & & \\ & 0 & & \cdots & A_{21}^{e-1} & A_{22}^e & A_{23}^e & \cdots & & 0 & \\ & & & & A_{31}^e & A_{32}^e & A_{33}^e + A_{11}^{e+1} & & & & \\ & \vdots & & & & \vdots & & \ddots & & \vdots & \\ & & & & & & & & A_{33}^{N_g-1} + A_{11}^{N_f} & A_{12}^{N_g} & A_{13}^{N_g} \\ & 0 & & & & 0 & & \cdots & A_{21}^{N_f} & A_{22}^{N_g} & A_{23}^{N_g} \\ & & & & & & & & A_{31}^{N_f} & A_{32}^{N_g} & A_{13}^{N_g} \end{bmatrix} \times \begin{bmatrix} E^1 \\ E^2 \\ E^3 \\ \vdots \\ E^{2(e-1)+1} \\ E^{2(e-1)+2} \\ E^{2(e-1)+3} \\ \\ E^{N_e-2} \\ E^{N_e-1} \\ E^{N_e} \end{bmatrix} = \begin{bmatrix} b^1 \\ 0 \\ 0 \\ \vdots \\ 0 \\ 0 \\ 0 \\ \vdots \\ 0 \\ 0 \\ b^{N_e} \end{bmatrix} \tag{10}$$

where the entries of matrix $[A]$ are given by:

$$A_{ij}^{e} = \int_{z_1^e}^{z_3^e} \left[\left(-\frac{1}{k_0} \underline{\underline{Q}}_H^{-1} \right) \frac{\mathrm{d}N_i^e(z)}{\mathrm{d}z} \cdot \frac{\mathrm{d}N_j^e(z)}{\mathrm{d}z} + k_0 \underline{\underline{Q}}_E N_i^e(z) N_j^e(z) \right] dz.$$

Solving equation (10) will give the electric field intensity along the z-direction.

2.2. *Absorbing boundary condition*

We can apply the absorbing boundary condition to the transmitted and reflected waves. For the perpendicularly polarized incident wave as shown in figure 2, the total wave at the boundary of both $z = z_0$ and $z = z_n$ is

$$\mathbf{E} = \mathbf{E}^{\mathrm{i}} + \mathbf{E}^{\mathrm{r}} \tag{11}$$

where the incident wave is

$$\mathbf{E}^{\mathrm{i}} = \exp(-\mathrm{j}k_z z) \cdot \mathbf{a}_y,$$

and the reflected wave is

$$\mathbf{E}^{\mathrm{r}} = \Gamma \exp(\mathrm{j}k_z z) \cdot \mathbf{a}_y.$$

From equation (11), the reflected wave at the boundary $z = z_0$ is:

$$\mathbf{E}^{\mathrm{r}} = \mathbf{E} - \mathbf{E}^{\mathrm{i}}. \tag{12}$$

If we take the differentiation of $\mathbf{E}^{\mathrm{r}}$ with respect to z, we have $\partial/\partial z\, \mathbf{E}^{\mathrm{r}} = \mathrm{j}k_z \mathbf{E}^{\mathrm{r}}$. Hence, by differentiating both sides of equation (11) with respect to z, we can obtain:

$$\frac{\partial}{\partial z}(\mathbf{E} - \mathbf{E}^{\mathrm{i}}) - \mathrm{j}k_z(\mathbf{E} - \mathbf{E}^{\mathrm{r}}) = 0$$

from which we get:

$$\frac{\partial}{\partial z} E_y \bigg|_{z=z_0} - \mathrm{j}k_z E_y|_{z=z_0} = -2\mathrm{j}k_z E_y^i|_{z=z_0}. \tag{13}$$

At the boundary $z = z_n$, since there is no reflection, the total wave is:

$$\mathbf{E} = \mathbf{E}^{\mathrm{t}}. \tag{14}$$

Using the same procedure as discussed before, we have:

$$\frac{\partial}{\partial z} E_y \bigg|_{z=z_n} + \mathrm{j}k_z E_y|_{z=z_n} = 0. \tag{15}$$

Likewise, we find the absorbing boundary condition of the parallel polarized incident wave as:

$$\begin{aligned} \frac{\partial}{\partial z} E_x \bigg|_{z=z_0} - \mathrm{j}k_z E_x|_{z=z_0} &= -2\mathrm{j}k_z E_x^{\mathrm{i}}|_{z=z_0} \\ \frac{\partial}{\partial z} E_x \bigg|_{z=z_n} + \mathrm{j}k_z E_x|_{z=z_n} &= 0. \end{aligned} \tag{16}$$

The circularly polarized wave can be composed from the linearly polarized waves as:

$$\begin{aligned} \mathbf{E}_{\mathrm{RCP}} &= (E_x \mathbf{a}_x + \mathrm{j}E_y \mathbf{a}_y)/2 \\ \mathbf{E}_{\mathrm{LCP}} &= (E_x \mathbf{a}_x - \mathrm{j}E_y \mathbf{a}_y)/2. \end{aligned} \tag{17}$$

2.3. *Reflectance and transmittance*

After solving the wave equations, the reflected and the transmitted waves can be obtained from equations (12) and (14), respectively. Hence, the reflectance of the TE, TM, LCP (left-hand circular polarization) and RCP waves at the boundary $z = z_0$ can be solved as

$$\begin{aligned} \Gamma_{\mathrm{TE}} &= E_y^{\mathrm{r}^2} / [(E_x^{\mathrm{i}}/\cos\theta)^2 + E_y^{\mathrm{i}^2}] \\ \Gamma_{\mathrm{TM}} &= (E_x^{\mathrm{r}}/\cos\theta)^2 / [(E_x^{\mathrm{i}}/\cos\theta)^2 + E_y^{\mathrm{i}^2}] \\ \Gamma_{\mathrm{LCP}} &= (E_x^{\mathrm{r}}/\cos\theta + \mathrm{j}E_y^{\mathrm{r}})^2 / [(E_x^{\mathrm{i}}/\cos\theta)^2 + E_y^{\mathrm{i}^2}] \\ \Gamma_{\mathrm{RCP}} &= (E_x^{\mathrm{r}}/\cos\theta - \mathrm{j}E_y^{\mathrm{r}})^2 / [(E_x^{\mathrm{i}}/\cos\theta)^2 + E_y^{\mathrm{i}^2}] \end{aligned} \tag{18}$$

where θ is the oblique incident angle.

The transmittance of TE, TM, LCP and RCP wave at the boundary $z = z_n$ can be found as

$$\begin{aligned} T_{\mathrm{TE}} &= E_y^{\mathrm{t}^2} / [(E_x^{\mathrm{i}}/\cos\theta)^2 + E_y^{\mathrm{i}^2}] \\ T_{\mathrm{TM}} &= (E_x^{\mathrm{t}}/\cos\theta)^2 / [(E_x^{\mathrm{i}}/\cos\theta)^2 + E_y^{\mathrm{i}^2}] \\ T_{\mathrm{LCP}} &= (E_x^{\mathrm{t}}/\cos\theta + \mathrm{j}E_y^{\mathrm{t}})^2 / [(E_x^{\mathrm{i}}/\cos\theta)^2 + E_y^{\mathrm{i}^2}] \\ T_{\mathrm{RCP}} &= (E_x^{\mathrm{t}}/\cos\theta - \mathrm{j}E_y^{\mathrm{t}})^2 / [(E_x^{\mathrm{i}}/\cos\theta)^2 + E_y^{\mathrm{i}^2}] \end{aligned} \tag{19}$$

2.4. *Glass and AR coating layers*

Reflection at the interface of air and LC occurs due to their dielectric constant difference. To minimize this reflection and make the simulation more realistic, both sides of the glass substrates are coated with six-layer anti-reflection (AR) films, as shown in figure 1. The AR coating films are designed with Binomial Transformer [12]. The dielectric constants $\varepsilon_\perp$ and $\varepsilon_\parallel$ are equal to each other inside the glass and AR coating layers so that equations (1) to (8) are still valid through the whole solution region.

3. Simulation results and discussions

3.1. *Comparison between the FEM and the 4 × 4-matrix method*

To validate the accuracy of the FEM model, we compare its results with those obtained by the 4×4 matrix method. The simulated Bragg reflection spectra using the 4×4 matrix method and the finite element method for the case of normal incidence are shown in figure 3 (*a*). The same comparison for the 20° oblique angle incidence inside the liquid crystal media is shown in figure 3 (*b*). For both methods, Bragg reflection spans about 60 nm bandwidth, centred at $\lambda_0 = 550$ nm for the normal incidence,

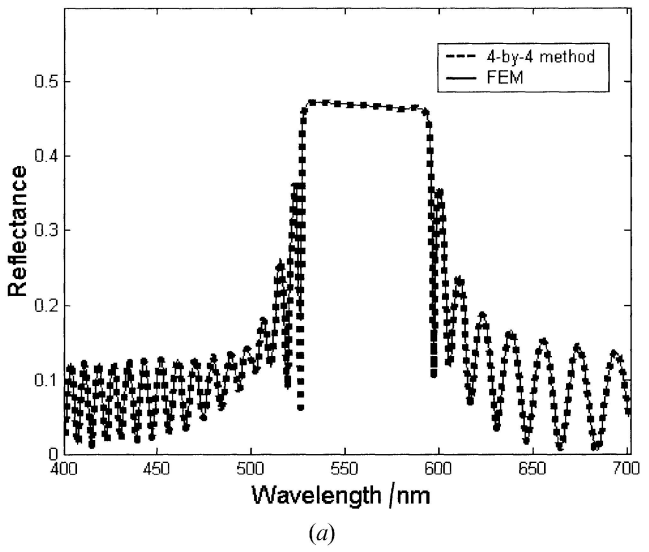

(*a*)

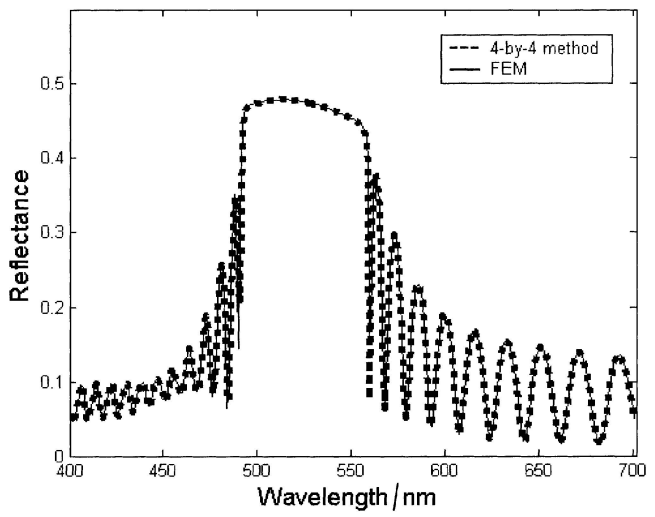

(*b*)

Figure 3. Comparison of Bragg reflection between the finite element method and the 4×4 matrix method: (*a*) normal incidence; (*b*) oblique incidence at 20° inside the LC layer. Ch-LC: $P_0 = 329\,\text{nm}$, $\Delta n = 0.2$ and $n_e = 1.8$. The FEM results overlap almost perfectly with those obtained from the 4×4 matrix method.

and centred at 525 nm for the 20° oblique incidence. In both simulations, the reflections from glass and LC interfaces are ignored. Our FEM results overlap perfectly with those obtained from the 4×4 method. The two results are almost indistinguishable.

3.2. *Central wavelength of Bragg reflection*

At the normal incidence, the helical pitches of the cholesteric LC layers introduce the Bragg reflection centred at wavelength λ_0 [1]:

$$\lambda_0 = nP_0 \tag{20}$$

where P_0 is the pitch length of the cholesteric liquid crystal and n is the average refractive index defined by [15–17]:

$$n^2 = (n_e^2 + 2n_0^2)/3. \tag{21}$$

For an oblique incidence wave propagating at an angle of Θ inside the liquid crystal, the central wavelength of Bragg reflection is governed by:

$$\lambda = nP_0 \cos \Theta \tag{22}$$

where Θ can be obtained by Snell's law as:

$$\Theta = \sin^{-1}\left(\frac{1}{n} \sin \theta\right). \tag{23}$$

The relationship between the angle Θ and the central wavelength of Bragg reflection is responsible for the blue shift [1, 4, 8].

3.3. *Broadband Bragg reflection*

Broadband Bragg reflection is highly desirable for electronic books and reflective polarizers as it will broaden the bandwidth and therefore enhance the display brightness. Another important application is that it will compensate for the blue shift shown in figure 4 if the bandwidth is sufficiently wide. The bandwidth of Bragg reflection is given by

$$\Delta\lambda = \Delta n P_0 \tag{24}$$

where $\Delta n = n_e - n_o$ is the birefringence of the liquid crystal. To expand the Bragg reflection to cover the entire visible region, two approaches are often considered. A straightforward method is to use a high birefringence LC.

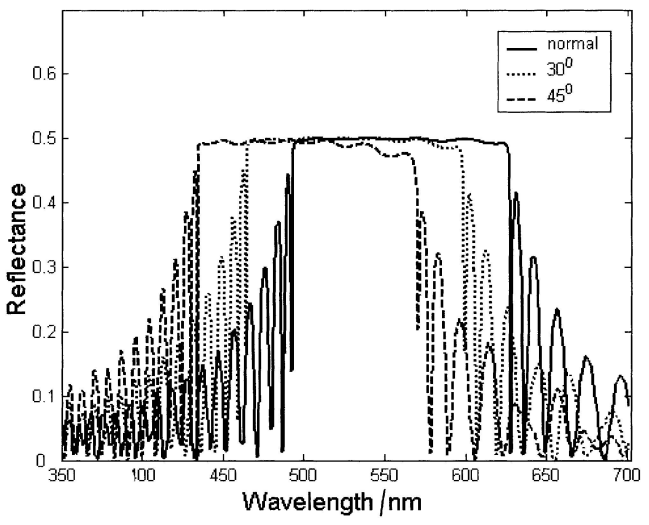

Figure 4. Blue shift on the Bragg reflection of a right-handed cholesteric LC. Ch-LC cell: $P_0 = 330\,\text{nm}$, $d = 16P_0$, $\Delta n = 0.4$ and $n_o = 1.5$. The glass substrates and AR coating layers are included in the calculations.

Two cholesteric liquid crystal materials with birefringence of 0.2 and 0.6 are compared in figure 5. The LC with $\Delta n \sim 0.2$ shows a 75 nm bandwidth. If the LC Δn is increased to 0.6, the reflection bandwidth is increased to ~ 200 nm. As the material research advances, LC compounds with $\Delta n > 0.5$ have been developed [1]. In these simulations, the LC cell gap is fixed at 16 P_0. The pitch length in each simulation is chosen so that the central wavelength of the Bragg reflection occurs at 550 nm.

An alternative approach to broaden reflection bandwidth is to use cholesteric liquid crystals with gradient pitch length. Figure 6 compares simulated results with pitch linearly varying from 240 to 350 nm (solid lines) and uniform pitch (dashed lines; $P_o = 310$ nm). In the former case, the bandwidth covers from 450 to 800 nm for the $\Delta n \sim 0.4$ LC employed. For the uniform pitch cell, the bandwidth (from 510 to 640 nm) is much narrower. However, in the gradient pitch approach, the interference of the liquid crystal chiral structure on the optical wave is not strong enough to establish Bragg reflection in the first few pitches. As a result, a thicker LC layer is needed. The drawback of a thick LC layer is its increased operating voltage.

In the gradient pitch approach, we have compared the linear and exponential pitch profiles. We assume the pitch grows from 240 to 350 nm within the cell gap. The gradients of the increased pitch length are given by:

$$P_{\text{linear}} = P_0 \cdot (1 + 0.458z/d)$$
$$P_{\text{exp}} = P_0 \exp(0.377z/d) \tag{25}$$

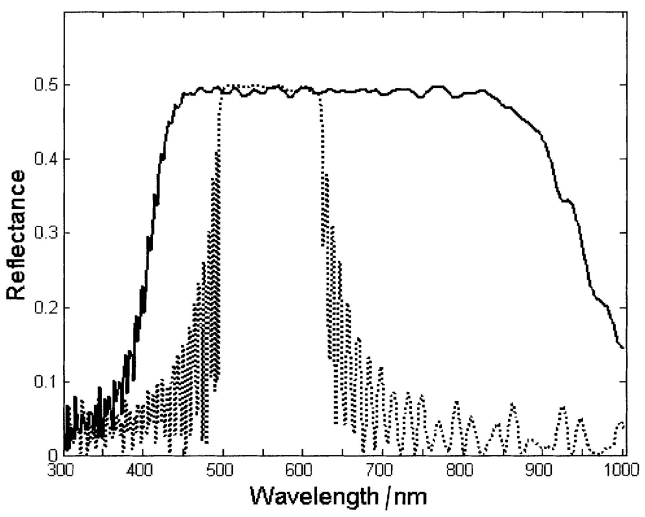

Figure 6. Bragg reflections of the right-hand Ch-LCs with uniform (dashed lines) and linearly increased (solid lines) pitch length. In both simulations, $\Delta n = 0.4$, $n_o = 1.6$, $d = 24P_0$ and $P_0 = 310$ nm. For the Ch-LC with linearly gradient pitch, P_0 increases from 240 to 350 nm as described in equation (25).

In equation (25), z and d are the direction coordinate and the LC cell gap, respectively, and $P_0 = 240$ nm. The simulation results are shown in figure 7. The cholesteric liquid crystal with exponentially increased pitch length profile provides somewhat wider bandwidth than the linearly increased case. However, the bandwidth of the peak Bragg reflection is rather similar; both cover from 420 to 900 nm.

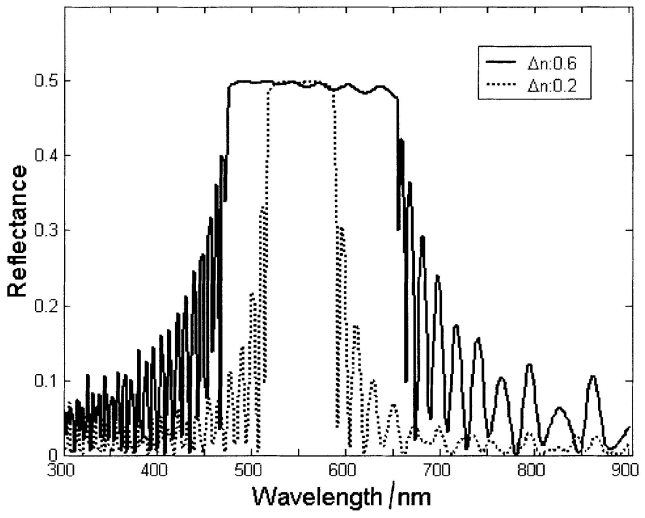

Figure 5. Bragg reflections of the right-hand cholesteric LCs with different birefringence at normal incidence. Ch-LC: uniform pitch length and $d = 16P_0$. The Δn of the LC materials is 0.2 and 0.6, and their ordinary refractive index is assumed to be 1.5 and 1.6, respectively. The pitch length in each simulation is set so that the central wavelength of the Bragg reflection is 550 nm.

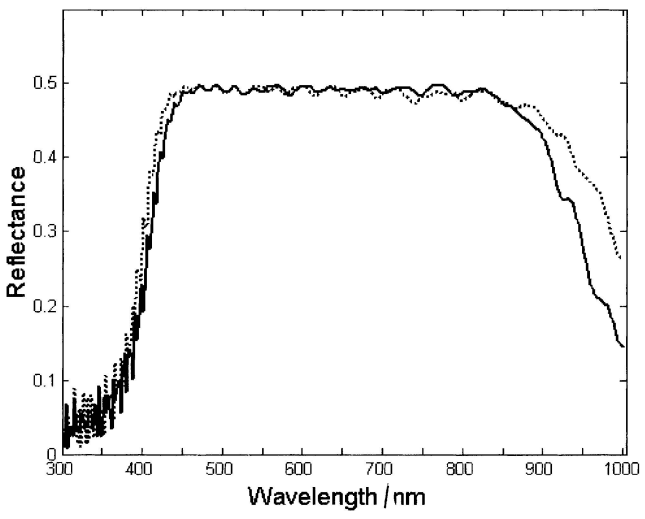

Figure 7. Comparison of Bragg reflections between Ch-LC with linearly (solid lines) and exponentially (dashed lines) increased pitch length. LC: $\Delta n = 0.4$ and $n_o = 1.6$, $d = 24P_0$ and $P_0 = 240$ nm. In both cases, the pitch length increases from 240 to 350 nm as described in equation (25).

From figure 7, the gradient pitch length technology dramatically increases the reflection bandwidth as compared with the traditional uniform pitch length approach. Thus, this method allows lower birefringence LC materials to be used for achieving a black and white Ch-LCD. The exponential pitch profile has been realized by UV treatment of the cholesteric LC sample containing photocurable monomer [18, 19].

3.4. *Establishment of Bragg reflection*

The strongly constructive interference of the reflected light inside the helical molecular structure is responsible for the observed Bragg reflection. In order to establish the Bragg reflection, a minimum cholesteric layer thickness is needed [1]. We have analysed such transient phenomena using FEM, and the simulation results are depicted in figure 8. For the uniform pitch cholesteric LC, Bragg reflection is established when the film thickness is larger than $10P_0$, where P_0 is the pitch length.

For a cholesteric liquid crystal with gradient pitch length, the pitch length is increased along the optical wave propagating direction. A thicker film is required in order to have sufficient pitches to establish the Bragg reflection. Figures 9 and 10 show the simulation results for the linear and exponential pitch profiles, respectively. In each case, an LC layer of more than $20P_0$ thickness is required for establishing the Bragg reflection. The required thickness of the liquid crystal film depends on the expected Bragg reflection spectrum and the pitch length profile. For a given LC mixture, a thicker cholesteric film would result in a higher operating voltage.

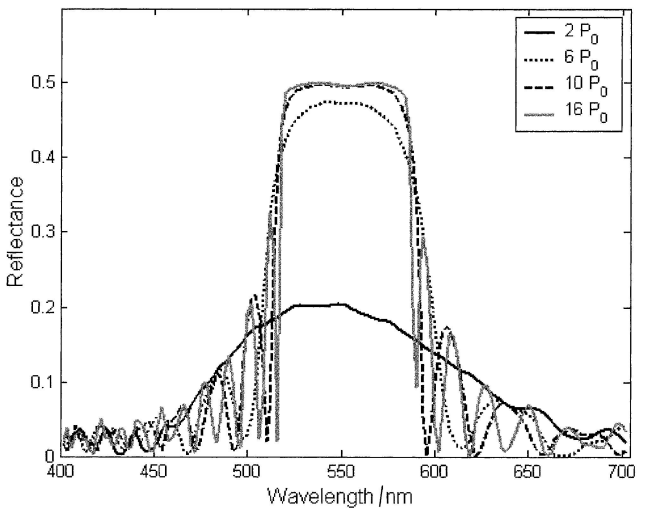

Figure 8. The establishment of Bragg reflection for a Ch-LC film with uniform pitch length at normal incidence. LC: $\Delta n = 0.4$, $n_o = 1.6$ and $P_0 = 310\,\text{nm}$.

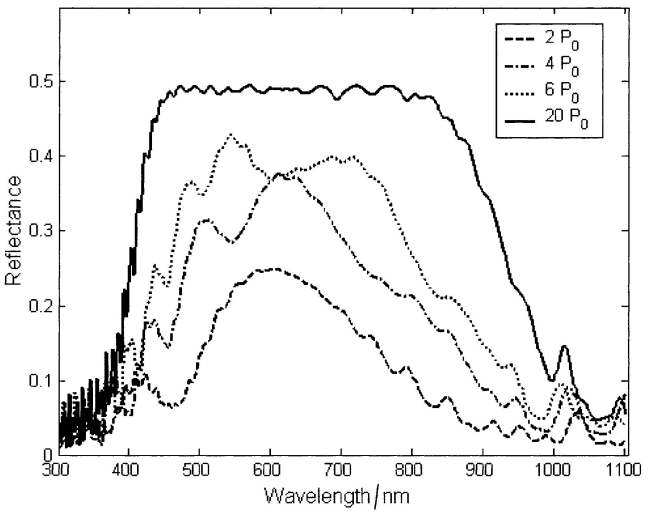

Figure 9. The establishment of Bragg reflection for a Ch-LC film with linearly increased pitch length at normal incidence. LC: $\Delta n = 0.4$, $n_o = 1.6$ and P_0 increases linearly from 240 to 350 nm as described in equation (25).

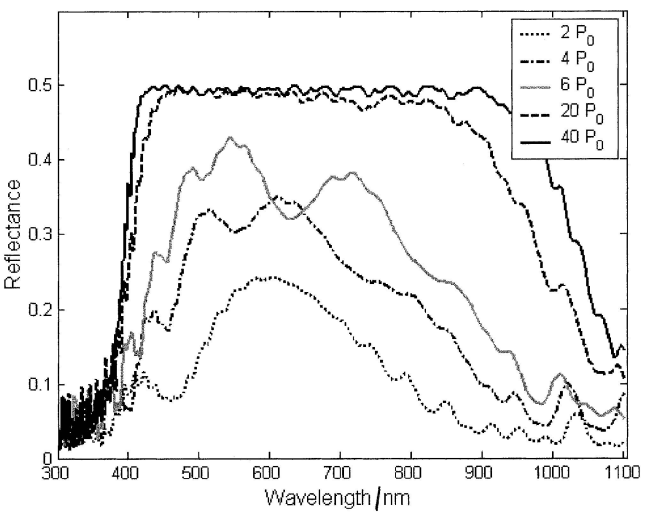

Figure 10. The establishment of Bragg reflection for a Ch-LC film with exponentially increased pitch length at normal incidence. LC: $\Delta n = 0.4$, $n_o = 1.6$, and P_0 increases from 240 to 350 nm exponentially as described in equation (25).

The results shown in figures 8–10 are for normal incidence. In oblique angle incidence, there is a strong coupling between the left-hand and right-hand circularly polarized waves when the wavelength reaches the Mauguin limit [1, 4, 8], as shown in figure 11. The profile of gradient pitch length enhances the coupling because of the short pitch length at the first few pitches. Furthermore, if the film is thicker the polarization coupling will be stronger, since there are more short pitch layers. When designing a cholesteric liquid crystal

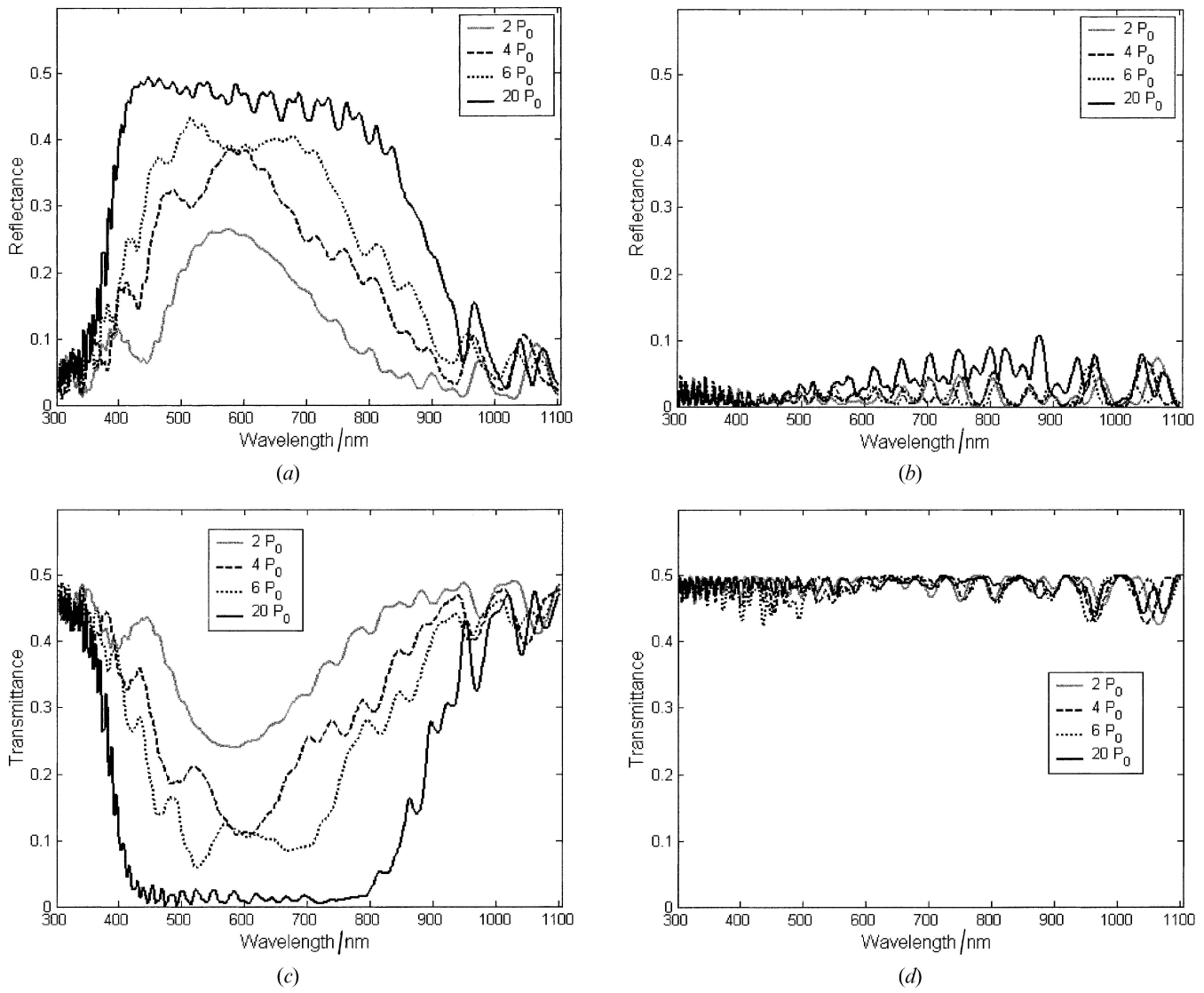

Figure 11. Polarization coupling of Bragg reflection for the Ch-LC with linearly increased pitch length at 30° viewing angle: (*a*) reflectance of the RCP wave; (*b*) reflectance of the LCP wave; (*c*) transmittance of the RCP wave; (*d*) transmittance of the LCP wave. LC: $\Delta n = 0.4$, $n_o = 1.6$ and P_0 increases linearly from 240 to 350 nm.

device, the balance between Bragg reflection bandwidth, film thickness, and polarization coupling in oblique angle incidence all need to be taken into consideration.

4. Conclusions

We have developed the finite element method for investigating the Bragg reflections of cholesteric liquid crystals. One-dimensional modelling of a cholesteric liquid crystal using the finite element method has been introduced. Two approaches for achieving broadband Bragg reflection have been analysed. The method of using a uniform pitch and high birefringence LC has the advantage of easy fabrication except that the required Δn is quite high. The gradient pitch method dramatically increases the bandwidth of Bragg reflection while the birefringence is relative smaller. Furthermore, the required LC film thickness has been investigated for the establishment of Bragg reflection as well as the polarization coupling of the oblique incidence waves.

The authors are indebted to AFOSR for financial support under contract No. F49620-01-1-0377.

References

[1] Wu, S. T., and Yang, D. K., 2001, *Reflective Liquid Crystal Displays* (New York: Wiley).
[2] Xu, M., Xu, F., and Yang, D. K., 1998, *J. appl. Phys.*, **83,** 1938.
[3] Yang, D. K., West, J. L., Chien, L. C., and Doane, J. W., 1994, *J. appl. Phys.*, **76,** 1331.

[4] Chandrasekhar, S., 1992, *Liquid Crystals* (Cambridge: Cambridge University Press).
[5] De Gennes, P. G., and Prost, J., 1993, *The Physics of Liquid Crystals* (Oxford: Oxford University Press).
[6] Khoo, I. C., and Wu, S. T., 1993, *Optics and Nonlinear Optics of Liquid Crystals* (Singapore: World Scientific).
[7] Drzaic, P. S., 1995, *Liquid Crystal Dispersions* (Singapore: World Scientific).
[8] Chigrinov, V. G., 1999, *Liquid Crystal Devices: Physics and Application* (Artech House).
[9] Blinov, L. M., 1983, *Electro-Optical and Magneto-Optical Properties of Liquid Crystals* (New York: Wiley).
[10] Berreman, D. W., 1972, *J. opt. Soc. Am.*, **62,** 502.
[11] Kwon, Y. W., 1997, *The Finite Element Method using MATLAB* (CRC Press).
[12] Volakis, J. L., Chatterjee, A., and Kempel, L. C., 1998, *Finite Element Method for Electromagnetics, Antennas, Microwave Circuits, and Scattering Applications* (Oxford: Oxford University Press).
[13] Balanis, C. A., 1989, *Advanced Engineering Electromagnetics* (New York: Wiley).
[14] Jing, J., 1993, *The Finite Element Method in Electromagnetics* (New York: Wiley).
[15] Wu, S. T., 1991, *J. appl. Phys.*, **69,** 2080.
[16] Wu, S. T., 1986, *Phys. Rev.*, **33,** 1270.
[17] Suh, S. W., Joseph, K., Cohen, G., Patel, J. S., and Lee, S. D., 1997, *Appl. Phys. Lett.*, **70,** 2547.
[18] Broer, D. J., 1995, *SID Dig.*, **26,** 165.
[19] Li, L., and Faris, S. M., 1996, *SID Dig.*, **27,** 111.